SPACE WEATHER, VOL. 8, S03006, doi:10.1029/2009SW000487, 2010

Geomagnetic influence on aircraft radiation exposure during a solar energetic particle event in October 2003

Christopher J. Mertens,[1] Brian T. Kress,[2] Michael Wiltberger,[3] Steve R. Blattnig,[1] Tony S. Slaba,[1,4] Stanley C. Solomon,[3] and M. Engel[5]

Received 24 April 2009; revised 19 December 2009; accepted 20 December 2009; published 25 March 2010.

[1] We present initial results from the Nowcast of Atmospheric Ionizing Radiation for Aviation Safety (NAIRAS) model during the Halloween 2003 superstorm. The objective of NAIRAS is to produce global, real-time, data-driven predictions of ionizing radiation for archiving and assessing the biologically harmful radiation exposure levels at commercial airline altitudes. We have conducted a case study of radiation exposure during a high-energy solar energetic particle (SEP) event in October 2003. The purpose of the case study is to quantify the important influences of the storm time and quiet time magnetospheric magnetic field on high-latitude SEP atmospheric radiation exposure. The Halloween 2003 superstorm is an ideal event to study magnetospheric influences on atmospheric radiation exposure since this event was accompanied by a major magnetic storm which was one of the largest of solar cycle 23. We find that neglecting geomagnetic storm effects during SEP events can underestimate the high-latitude radiation exposure from nearly 15% to over a factor of 2, depending on the flight path relative to the magnetosphere open-closed boundary.

Citation: Mertens, C. J., B. T. Kress, M. Wiltberger, S. R. Blattnig, T. S. Slaba, S. C. Solomon, and M. Engel (2010), Geomagnetic influence on aircraft radiation exposure during a solar energetic particle event in October 2003, *Space Weather*, *8*, S03006, doi:10.1029/2009SW000487.

1. Introduction

[2] An important atmospheric state variable, driven by space weather phenomena, is the ionizing radiation field. The two sources of atmospheric ionizing radiation are (1) the ever present, background galactic cosmic rays (GCR), with origins outside the solar system, and (2) the transient solar energetic particle (SEP) events, which are associated with eruptions on the Sun's surface lasting for several hours to days with widely varying intensity. Quantifying the levels of atmospheric ionizing radiation is of particular interest to the aviation industry since it is the primary source of human exposure to high linear energy transfer (LET) radiation. This radiation is effective at directly breaking DNA strands in biological tissue, or producing chemically active radicals in tissue that alter the cell function, both of which can lead to cancer or other adverse health effects. Consequently, there is increased concern about potential health outcomes among passengers and crew in the commercial and private aviation sector [*Wilson et al.*, 2005b, 2003]. As a result, there is a growing need for a capability to predict the real-time radiation levels at airline altitudes in order to (1) provide a continuous assessment of ionizing radiation exposure for tracking aircrew exposure levels, (2) provide time-critical data during SEP events for aviation radiation risk evaluation and mitigation, and (3) provide an archived database of radiation exposure for assessing the impact of ionizing radiation on the global air transportation system as a whole, especially in view of the current and future exponential growth in the number of polar routes. The polar region receives the largest quantity of radiation because the shielding provided by Earth's magnetic field rapidly approaches zero near the magnetic pole.

[3] Currently under development is the Nowcast of Atmospheric Ionizing Radiation for Aviation Safety (NAIRAS) model [*Mertens et al.*, 2008]. The goal of NAIRAS is to provide a data-driven, global, real-time prediction of ionizing radiation exposure from the surface to approxi-

[1]NASA Langley Research Center, Hampton, Virginia, USA.
[2]Department of Physics and Astronomy, Dartmouth College, Hanover, New Hampshire, USA.
[3]High Altitude Observatory, National Center for Atmospheric Research, Boulder, Colorado, USA.
[4]Department of Mathematics and Statistics, Old Dominion University, Norfolk, Virginia, USA.
[5]Department of Physics, Hamline University, Saint Paul, Minnesota, USA.

mately 100 km. NAIRAS has adopted, as far as possible, the meteorological weather forecasting paradigm of combining physics-based forecast models with data assimilation techniques. The physics-based model we use to transport the ionizing radiation through the atmosphere and calculate the dosimetric quantities is the High charge (Z) and Energy Transport (HZETRN) code [*Wilson et al.*, 1991]. While the quantity of observations relevant to radiation exposure predictions is currently too sparse to apply data assimilation techniques per se, nevertheless, we utilize as much real-time measurement data as possible to characterize the sources of ionizing radiation incident at the top of the atmosphere and the material properties of the atmosphere necessary to understand the transport and transmutations of the sources of ionizing radiation through the atmosphere.

[4] There are a number of models currently in use for calculating GCR radiation exposure at aircraft altitudes. The CARI-6 model utilizes a database of transport calculations generated by the deterministic LUIN code for a wide variety of geographic locations, altitudes, and solar activity levels [*O'Brien et al.*, 2003, 1998]. The EPCARD model is based on a similar approach, but uses the Monte Carlo FLUKA code for the transport calculations [*Schraube et al.*, 1999]. PC-AIRE is a semiempirical model based on fits to measurement data [*Lewis et al.*, 2002]. Other aircraft radiation exposure models are described in the recent European Radiation Dosimetry Group report [*Lindborg et al.*, 2004]. Currently, the above models calculate SEP atmospheric radiation exposure poststorm on a case-by-case basis, although PC-AIRE incorporated low-Earth orbit measurements to develop a simple extrapolation to SEP events [*Lewis et al.*, 2002]. Recently, *Copeland et al.* [2008] calculated adult and conceptus aircraft exposure rates for 170 SEP events for years 1986–2008 using the Monte Carlo MCNPX transport code.

[5] The main differences that distinguish the NAIRAS model from the models discussed above are the following. The physics-based deterministic HZETRN transport calculations used in NAIRAS are continuously updated using real-time measurements of the space radiation environment and of atmospheric density versus altitude. Furthermore, both GCR and SEP atmospheric radiation exposure predictions are included in real time. And finally, dynamical geomagnetic effects are routinely included in the NAIRAS radiation exposure calculations.

[6] In this paper we conduct a case study and focus solely on SEP aircraft radiation exposure during the Halloween 2003 superstorm. The specific time interval analyzed is from 29 October (2100 UT) through 31 October (2400 UT). The primary objective of this case study is to diagnose the influence of geomagnetic storm effects on SEP atmospheric radiation exposure. The interest in understanding aviation ionizing radiation, and SEP exposure in particular, is because the International Commission on Radiological Protection (ICRP), the Environmental Protection Agency (EPA), and the Federal Aviation Administration (FAA) consider crews of commercial aircraft as radiation workers [*McMeekin*, 1990; *ICRP*, 1991]. However, aircrew are currently not monitored for radiation exposure, nor are passengers aware of any potential radiation risks. Reproductive disorder, including prenatal injury, are a particular concern [*Lauria et al.*, 2006; *Waters et al.*, 2000; *Aspholm et al.*, 1999].

[7] The importance of our case study is that we find geomagnetic storm effects to have a profound effect on SEP atmospheric radiation exposure. The Halloween 2003 superstorm is an ideal event to study geomagnetic effects since this event contained a major magnetic storm which was one of the largest of solar cycle 23. The geomagnetic storm effects are the consequence of solar wind–magnetosphere interactions that weaken the effective shielding of incident low-energy SEP ions by the Earth's magnetic field [*Kress et al.*, 2010]. The effect of a weakened magnetic field, in response to a geomagnetic storm, is a significant increase in SEP atmospheric ionizing radiation. This result underscores the need for continued space environment measurements and accurate models of solar wind–magnetosphere interactions.

[8] The outline of the rest of the paper is as follows. In section 2 we describe the measurement data and space environment models used to characterize the incident SEP particle flux at the top of the atmosphere, and the meteorological data and models used to characterize atmospheric density. Section 3 describes the transport of the incident SEP ion flux through the atmosphere and the calculation of radiation exposure. The high-energy SEP event during the Halloween 2003 superstorm is analyzed in section 4. A summary and conclusions are presented in section 5.

2. Data Input and Space Environment Models

[9] NAIRAS model predictions of atmospheric SEP radiation exposure are driven by measurements from the atmosphere and from space. Real-time satellite ion flux measurements are used to derive the SEP proton and alpha spectral fluence rates incident at the top of the atmosphere. The geomagnetic field (internal field plus magnetospheric contributions) filters the incident SEP spectral fluence rates by deflecting the lower-energy particles back out to space. This spectral filtering effect is quantified by a canonical variable called the geomagnetic cutoff rigidity. Satellite measurements of solar wind dynamical pressure and the interplanetary magnetic field (IMF) are used to characterize the magnetospheric contributions to the cutoff rigidity. Global meteorological measurements combined with data assimilation and forecast models are used to predict atmospheric depth as a function of altitude. In sections 2.1–2.3, we describe the data input and space environment models used to derive (1) the incident SEP spectral fluence rates, (2) the geomagnetic cutoff rigidity, and (3) atmospheric depth as a function of altitude.

2.1. SEP Spectral Fluence Rates

[10] The current understanding of SEP processes is that the energy spectrum is a result of injected particle seed

populations that are stochastically accelerated in a turbulent magnetic field associated with a CME-driven interplanetary shock [*Tylka and Lee*, 2006]. An analytical expression that represents the differential energy spectrum for this shock acceleration mechanism was given by *Ellison and Ramaty* [1985], where the spectrum has the form

$$\frac{d^2J}{dEd\Omega} = C_a E^{-\gamma_a} \exp(-E/E_0). \quad (1)$$

The differential energy spectrum on the left-hand side of (1) has units of cm^{-2} sr^{-1} h^{-1} $(MeV/n)^{-1}$, and the energy (E) has units of MeV n^{-1} (i.e., MeV per nucleon). The constant C_a is related to the injected seed population far upstream of the shock. The power law energy dependence of the spectrum is due to shock acceleration of the seed population by random first-order Fermi acceleration (scattering) events in a turbulent magnetic field, with the power index (γ_a) related to the shock compression ratio. The exponential turnover in (1) represents high-energy limits to the acceleration mechanism, such as escape from the shock region. Using the above analytical form, the three parameters (C_a, γ_a, and E_0) can be determined by fitting (1) to ion flux measurements.

[11] Recently, *Mewaldt et al.* [2005] found that the Ellison-Ramaty spectral form failed to fit NOAA/GOES ion flux measurements at the highest-energy channels during the Halloween 2003 SEP events. To circumvent this deficiency, Mewaldt et al. proposed using a double power law spectrum. The low-energy spectrum is assumed to follow the Ellison-Ramaty form. The high-energy spectrum is assumed to have a power law energy dependence with a different power index, such that

$$\frac{d^2J}{dEd\Omega} = C_b E^{-\gamma_b}. \quad (2)$$

The power law expressions in (1) and (2) can be merged into one continuous spectrum by requiring that the differential energy spectra in (1) and (2) and their first derivatives are continuous at the merge energy. The result is given by the expression below:

$$\frac{d^2J}{dEd\Omega} = C E^{-\gamma_a} \exp(-E/E_0), E \le (\gamma_b - \gamma_a)E_0 \quad (3)$$

$$= C E^{-\gamma_b} \left\{ [(\gamma_b - \gamma_a)E_0]^{(\gamma_b - \gamma_a)} \exp(\gamma_b - \gamma_a) \right\}, \quad E > (\gamma_b - \gamma_a)E_0. \quad (4)$$

Physically, the double power law spectrum in (3) and (4) represents SEP sources from two different injected seed populations. For example, the low-energy spectrum, with γ_a power index and the e-folding energy E_0, is likely associated with solar corona (solar wind) seed populations while the high-energy spectrum, with γ_b power index, is likely associated with flare suprathermal seed populations [*Tylka et al.*, 2005].

[12] The NAIRAS model initially assumes the double power law form in (3) and (4) for the SEP fluence spectrum and derives the fit parameters (C, γ_a, γ_b, and E_0) by a nonlinear least squares fit to differential-directional ion flux measurements. The spectral fitting algorithm uses a Marquardt-Levenberg iteration technique [*Brandt*, 1999]. If the double power law spectrum fails to converge to the measurement data, the fitting procedure is restarted and the Ellison-Ramaty spectral form is assumed.

[13] NAIRAS utilizes available real-time measurements of proton and alpha differential-directional particle flux (cm^{-2} sr^{-1} s^{-1} $(MeV/n)^{-1}$) for the SEP spectral fitting described above. SEP spectral fluence rates (cm^{-2} h^{-1} $(MeV/n)^{-1}$) incident on Earth's atmosphere are obtained by time averaging the particle flux measurements in 1 h time bins and projecting the incident flux onto the vertical direction assuming an isotropic angular distribution for the solar ions. Low-energy proton data are obtained from the Electron, Proton, and Alpha Monitor (EPAM) instrument onboard the NASA Advanced Composition Explorer (ACE) satellite [*Gold et al.*, 1998]. EPAM is composed of five telescopes and we use the LEMS120 (Low-Energy Magnetic Spectrometer) detector, which measures ions at 120 degrees from the spacecraft axis. LEMS120 is the EPAM low-energy ion data available in real time, for reasons described by *Haggerty et al.* [2006]. The other proton channels used in the SEP spectral fitting algorithm are obtained from NOAA's Geostationary Operational Environmental Satellite (GOES) Space Environment Monitor (SEM) measurements. The Energetic Particle Sensor (EPS) and the High Energy Proton and Alpha Detector (HEPAD) sensors on GOES/SEM measure differential-directional proton flux [*Onsager et al.*, 1996]. We also generate additional differential-directional proton flux measurement channels by taking differences between the EPS integral proton flux channels. The channels used to derive SEP alpha spectral fluence rates are also obtained from EPS measurements. We use 5 min averaged ACE and GOES data to derive the incident SEP spectral fluence rates.

[14] Figure 1 shows the time variation of a representative set of proton flux measurements used to derive incident SEP spectral fluence rates for the Halloween 2003 storm period. The two plots show the GOES 11 EPS and HEPAD proton flux spectra and the integral proton flux measurements. By definition, a SEP event occurs when the >10 MeV integral proton flux exceeds 10 proton flux units (pfu ≡ cm^{-2} sr^{-1} s^{-1}) in three consecutive 5 min periods [*NOAA*, 2009]. The SEP event threshold is denoted by the horizontal line in the integral proton flux plot (Figure 1, bottom). There are a total of five SEP events during the Halloween 2003 storm period, which are denoted by the vertical lines in both plots in Figure 1. These events were associated with many simultaneous, complex phenomena such as solar flares, coronal mass ejections (CME), interplanetary shocks, and solar cosmic ray ground level enhancements (GLE) [see *Gopalswamy et al.*, 2005]. Different

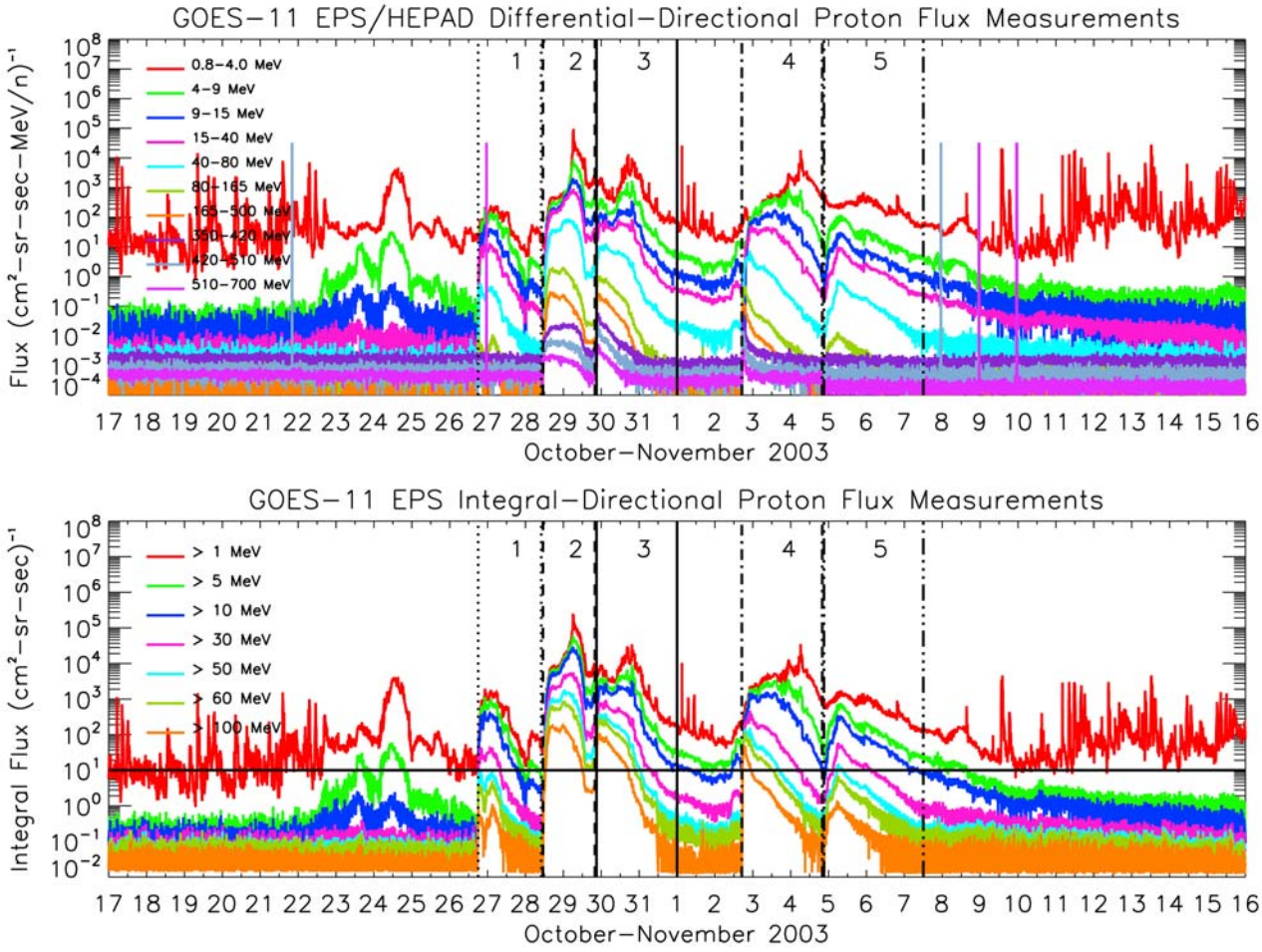

Figure 1. GOES 11 proton flux measurements: (top) the EPS/HEPAD differential-directional flux and (bottom) the EPS integral-directional flux. The color lines represent different GOES 11 proton channels, and the energy ranges of the channels are specified in the legend. The different vertical line styles bound the five SEP events, which are also numbered in both plots. See text for details.

line styles are used to bound each of the five events, and the event number is shown between the vertical lines. Note that the onset of event 3 does not follow the conventional SEP threshold definition. It is clear from the integral proton flux that two events overlap: event 3 arrives before event 2 decreases below the SEP threshold level. However, there is an important distinguishing feature between the two events. That is, the beginning of our definition of event 3 is accompanied by a sudden increase in high-energy protons associated with the arriving SEP event, as noted by the sudden increase in the 510–700 MeV differential-directional proton flux measurements in Figure 1. Partitioning the simultaneous SEP events 2 and 3 into separate events is useful for our study, since the high-energy portion of the differential-directional proton flux distribution penetrates deeper in the atmosphere.

[15] We will analyze atmospheric ionizing radiation exposure during SEP event 3 (29 October (2100 UT) to 31 October (2400 UT)) since the associated interaction between the arriving CME-driven interplanetary shock and Earth's magnetosphere caused the largest geomagnetic effects during the Halloween 2003 storm period, which is the focus of our case study. In order to isolate the geomagnetic effects, we derived the event-averaged SEP spectral fluence rates shown in Figure 2. The horizontal lines in Figure 2 are the event-averaged differential-directional ion flux measurements. The width of the horizontal lines correspond to the energy width of the measurement channels. The black lines are the proton and alpha spectral fluence rates derived using the double power law spectrum and fitting technique describe above. The shaded regions show the range of 1 h averaged ion flux measurements in the time interval of event 3. The peach colored region corresponds to the range of proton flux measurements and the blue colored region corresponds to the alpha flux measurements The event-averaged fit parameters derived

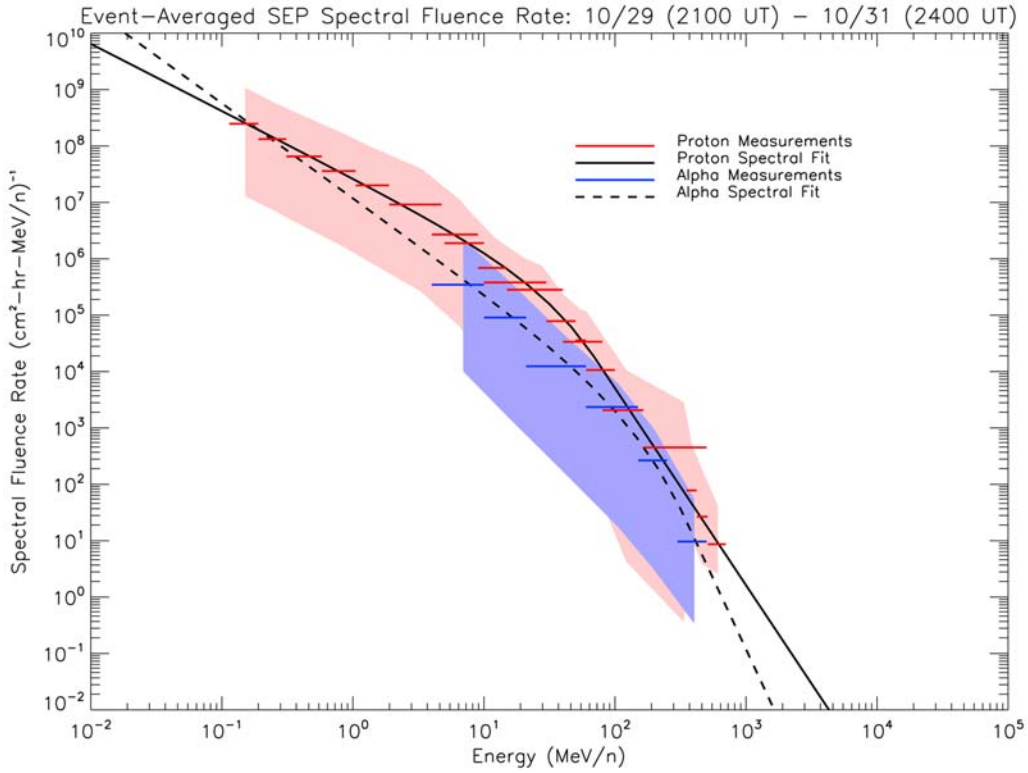

Figure 2. Event-averaged SEP spectral fluence rates for event 3 (29 October 2003 (2100 UT) to 31 October 2003 (2400 UT)). The shaded regions show the range of 1 h averaged ion flux measurements in the time interval of event 3. The peach shaded region corresponds to proton flux measurements. The blue shaded region corresponds to the alpha flux measurements.

for SEP event 3 are given in Table 1. Thus, equations (3) and (4) and the parameters in Table 1 characterize the incident SEP spectral fluence rates used in the analysis of atmospheric exposure in this paper. One can readily reproduce our incident SEP spectral fluence rate and compare with our computed exposure rates presented in section 4.

2.2. Geomagnetic Cutoff Rigidities

[16] The geomagnetic field provides a form of momentum shielding by deflecting lower-energy charged particles back out to space. The minimum momentum per unit charge that a vertically incident particle can have and still reach a given altitude above the Earth is called the vertical geomagnetic cutoff rigidity. The cutoff rigidity is a canonical variable for specifying the minimum access energy of incident charged particles (SEP particles in this study) for transport through the atmosphere. Once the cutoff rigidity is known, the minimum access energy is determined for each incident particle of charge Z and mass number A through the relativistic energy equation, such that

$$E = \left[\sqrt{R^2(Z/A \cdot \text{amu} \cdot c^2)^2 + 1} - 1\right] \cdot \text{amu} \cdot c^2, \qquad (5)$$

where E is kinetic energy per nucleon (MeV n^{-1}), R is vertical geomagnetic cutoff rigidity (MV), c is the speed of light in vacuum, and amu = 931.5 MeV c^{-2} (atomic mass unit).

[17] The cutoff rigidity is determined by numerical solution of charged particle trajectories in the geomagnetic field [*Smart and Shea*, 2005, 1994]. The NAIRAS cutoff rigidities are calculated from code developed by the Center for Integrated Space Weather Modeling (CISM) at Dartmouth College. The CISM, Dartmouth geomagnetic cutoff model can be run using several different empirical and physics-based models [*Kress et al.*, 2004]. In particular, the specification of the geomagnetic field due to Earth's internal field source is provided by the International Geomagnetic Reference Field (IGRF) model [*Langlais and Mandea*, 2000]. The

Table 1. Event-Averaged Fit Parameters[a]

Particle	C	γ_a	γ_b	E_0
Proton	8.565×10^6	1.191	3.493	30.78
Alpha	3.782×10^6	1.682	4.992	105.3

[a]Event is from 29 October 2003 (2100 UT) to 31 October 2003 (2400 UT).

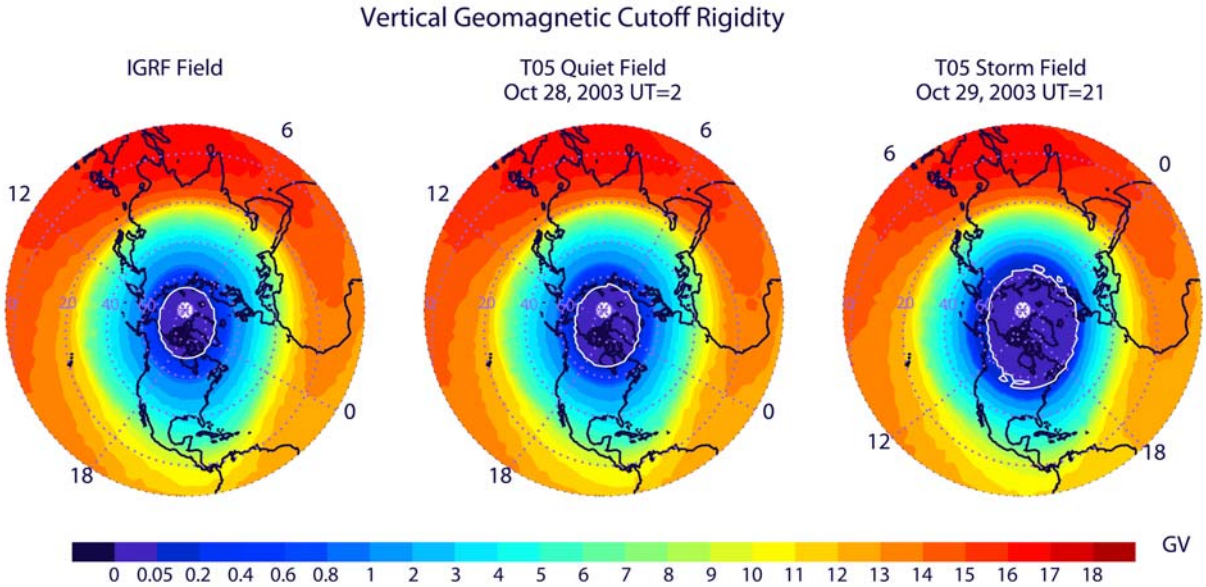

Figure 3. Simulated vertical geomagnetic cutoff rigidity shown over the Northern Hemisphere in October 2003. The cutoff rigidities were calculated using (left) the IGRF model, (middle) the T05 model during a geomagnetically quiet period, and (right) the T05 model during the largest geomagnetically disturbed period of SEP event 3. Also shown are the magnetic latitude circles and the meridians at 0000, 0600, 1200, and 1800 magnetic local time.

IGRF 2000 epoch is used in this study. The magnetospheric current systems are also important contributors to Earth's total geomagnetic field. The real-time dynamical response of the magnetospheric magnetic field to solar wind conditions and IMF can be provided by the semiempirical T05 model [*Tsyganenko and Sitnov*, 2005], or by the Lyon-Feder-Mobarry (LFM) global MHD simulation code [*Lyon et al.*, 2004]. Currently, the T05 model provides more accurate cutoff rigidities than the LFM MHD model, as determined by comparisons with satellite observations during a Halloween 2003 geomagnetic storm [*Kress et al.*, 2010]. Thus, for the present work, the simulated real-time geomagnetic cutoff rigidities are calculated using the T05 model, and using the IGRF model for comparison.

[18] Figure 3 shows the vertical cutoff rigidity over the Northern Hemisphere for three different models of the geomagnetic field. Figure 3 (left) is cutoff rigidity computed using the IGRF field. Since total flight path exposures at aviation altitudes do not change significantly (<~1%) for cutoffs less than 0.05 GV, we set the cutoffs to zero at geographic locations poleward of the 0.05 GV contour (see the bold white 0.05 GV color contour in Figure 3). Figure 3 (middle) shows the cutoff rigidities computed using the T05 field under geomagnetically quiet conditions, 28 October (0200 UT), prior to the onset of the Halloween 2003 SEP event 3. One can see that even during magnetically quiet conditions, the cutoff rigidities predicted from the T05 field are lower than predicted from the IGRF field, and the polar cap region (i.e., inside the bold white 0.05 GV contour in Figure 3) is expanded to lower latitudes. A weaker field predicted by the T05 model, compared to IGRF, is due in part to the diamagnetic effect of the magnetospheric ring current included in the T05 model. Lower cutoff rigidities correspond to less momentum shielding and higher radiation exposure levels. Figure 3 (right) shows the cutoff rigidities during peak geomagnetic storm conditions, 29 October (2100 UT), during SEP event 3. The cutoffs are lower at all latitudes compared to the two previous simulations, and the polar cap region has expanded to much lower latitudes than during the magnetically quiet period. These geomagnetic effects are discussed in more detail in section 4.

2.3. Atmospheric Depth Altitude

[19] The atmosphere itself provides shielding from incident charged particles. The shielding of the atmosphere at a given altitude depends on the overhead mass. Subdaily global atmospheric depth is determined from pressure versus geopotential height and pressure versus temperature data derived from the National Center for Environmental Prediction (NCEP)/National Center for Atmospheric Research (NCAR) Reanalysis 1 project [*Kalnay et al.*, 1996]. The NCAR/NCEP Reanalysis 1 project uses a state-of-the-art analysis/forecast system to perform data assimilation using past data from 1948 to the present. The data products are available 4X daily at 0000, 0600, 1200, and 1800 UT. The spatial coverage is 17 pressure levels in the vertical from approximately the surface (1000 hPa) to the

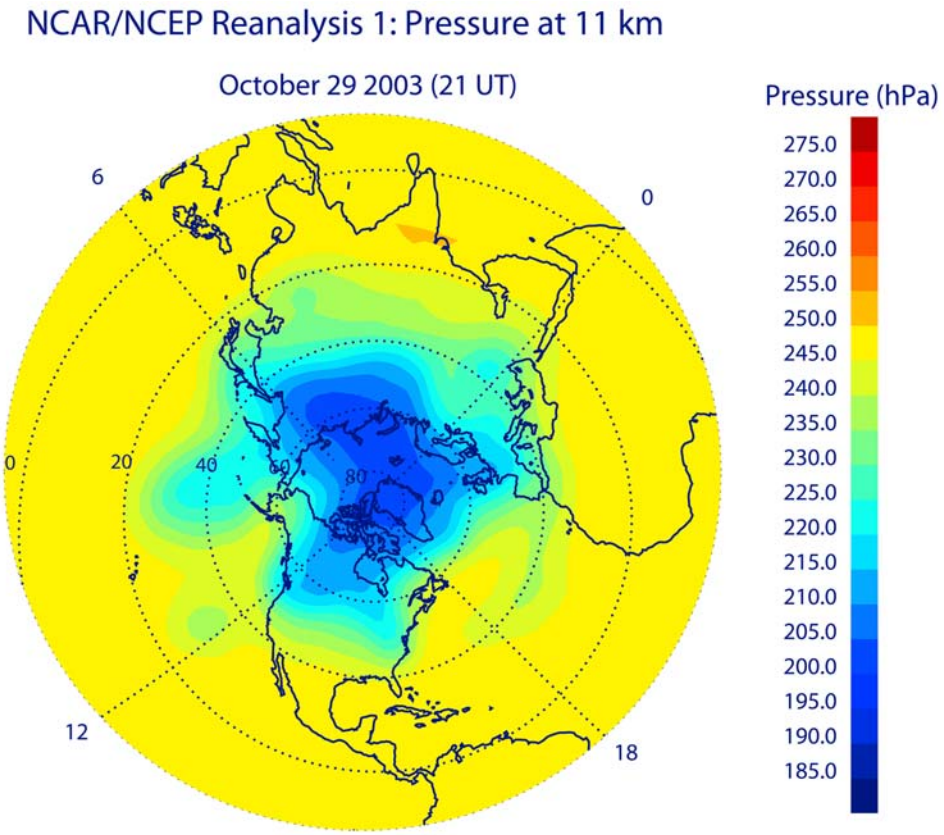

Figure 4. NCAR/NCEP Reanalysis 1 pressure levels at 11 km corresponding to the date/time of the largest geomagnetically disturbed period of SEP event 3 (29 October 2003, 2100 UT). Also shown are the magnetic latitude circles and the meridians at 0000, 0600, 1200, and 1800 magnetic local time.

middle stratosphere (10 hPa), while the horizontal grid is 2.5 × 2.5 degrees covering the entire globe.

[20] NCAR/NCEP pressure versus geopotential height data is extended in altitude above 10 hPa using the Naval Research Laboratory Mass Spectrometer and Incoherent Scatter (NRLMSIS) model atmosphere [*Picone et al.*, 2002]. NCAR/NCEP and NRLMSIS temperatures are smoothly merged at 10 hPa at each horizontal grid point. NRLMSIS temperatures are produced at 2 km vertical spacing from the altitude of the NCEP/NCAR 10 hPa pressure surface to approximately 100 km. The pressure at these extended altitudes can be determined from the barometric law using the NRLMSIS temperature profile and the known NCAR/NCEP 10 hPa pressure level, which assumes the atmosphere is in hydrostatic equilibrium and obeys the ideal gas law. Finally, the altitudes and temperatures are linearly interpolated in log pressure to a fixed pressure grid from 1000 hPa to 0.001 hPa, with six pressure levels per decade. The result from this step is pressure versus altitude at each horizontal grid point from the surface to approximately 100 km.

[21] Atmospheric depth (g cm^{-2}) at each altitude level and horizontal grid point is computed by vertically integrating the mass density from a given altitude to the top of the atmosphere. The mass density is determined by the ideal gas law using the pressure and temperature at each altitude level. The result from this step produces a 3-D gridded field of atmospheric depth. Atmospheric depth at any specified aircraft altitude is determined by linear interpolation along the vertical grid axis in log atmospheric depth. Figure 4 shows the atmospheric pressure over the Northern Hemisphere at 11 km on 29 October 2003 (2100 UT). This is the atmospheric data used in the exposure rate calculations in section 4.

3. SEP Transport and Dosimetry

[22] In section 2, we described the incident SEP spectral fluence rates, cutoff rigidity, and atmospheric depth as a function of altitude. In this section, we describe the transport of the incident SEP ions through the atmosphere and the subsequent absorbed dose in tissue from the ionizing radiation field.

[23] SEP atmospheric transport is described by a coupled system of linear Boltzmann transport equations, which are derived on the basis of conservation principles [*Wilson et*

al., 1991]. The transport equation for the spectral fluence rate $\phi_j(\mathbf{x}, \mathbf{\Omega}, E)$ for particle type j is given by

$$\mathbf{\Omega} \bullet \nabla \Phi_j(\mathbf{x}, \mathbf{\Omega}, E) = \sum_k \int \sigma_{jk}\left(\mathbf{\Omega}, \mathbf{\Omega}', E, E'\right) \Phi\left(\mathbf{x}, \mathbf{\Omega}', E'\right) d\mathbf{\Omega}' dE' - \sigma_j(E) \Phi(\mathbf{x}, \mathbf{\Omega}, E), \quad (6)$$

where $\sigma_j(E)$ and $\sigma_{jk}(\mathbf{\Omega}, \mathbf{\Omega}', E, E')$ are the target medium macroscopic cross sections. The $\sigma_{jk}(\mathbf{\Omega}, \mathbf{\Omega}', E, E')$ are double-differential particle production cross sections that represent all processes by which type k particles moving in direction $\mathbf{\Omega}'$ with energy E' produce a particle of type j moving in direction $\mathbf{\Omega}$ with energy E, including radioactive decay processes. The total cross section $\sigma_j(E)$ of the target medium for each incident particle type j is

$$\sigma_j(E) = \sigma_{j,at}(E) + \sigma_{j,el}(E) + \sigma_{j,r}(E), \quad (7)$$

where the first term refers to collisions with atomic electrons, the second term refers to elastic ion-nucleus scattering, or elastic neutron-neutron scattering, and the third term contains all relevant nuclear reactions. The corresponding differential cross sections are similarly ordered.

[24] The coupled SEP transport equations in (6) are solved in the NAIRAS model using NASA Langley Research Center's deterministic HZETRN code. HZETRN is used in a wide variety of radiation transport applications, e.g., the calculation of dosimetric quantities for assessing astronaut risk to space radiations on the International Space Station (ISS) and the Space Transportation System (STS) Shuttle, and for design and validation of the Crew Exploration Vehicle (CEV) under the Constellation program, including realistic spacecraft and human geometry [*Slaba et al.*, 2009; *Badavi et al.*, 2007a, 2005; *Wilson et al.*, 2006]. Extensive summaries of HZETRN laboratory and space flight verification and validation are found in recent reports by *Badavi et al.* [2007a], *Nealy et al.* [2007], and *Wilson et al.* [2005a, 2005c].

[25] For SEP proton and alpha particles incident at the top of the atmosphere, solutions to six coupled transport equations are obtained: one for neutrons and five for light ions (protons, deuterons, tritons, helium-3, and helium-4). A recent update to HZETRN includes a directionally coupled forward-backward low-energy neutron transport algorithm, which is important for atmospheric radiation transport (T. C. Slaba et al., Coupled neutron transport for HZETRN, submitted to *Advances in Space Research*, 2008).

[26] The energy deposited in a target medium by the radiation field of particle j is the dose, which is given by

$$D_j(\mathbf{x}) = K \int_{\Omega} \int_0^{\infty} S_j(E) \Phi_j(\mathbf{x}, \mathbf{\Omega}, E) d\mathbf{\Omega} dE. \quad (8)$$

In the above equation, $S_j(E)$ is the target stopping power for particle j (Mev g^{-1} cm^{-2}) and K is a unit conversion factor (1.602×10^{-10}) to convert dose to units of Gray (1 Gy = J kg^{-1}). Radiation health risk and the probability of biological damage depend not only on the absorbed dose, but also on the particle type and energy of the radiation causing the dose. This is taken into account by weighting the absorbed dose by a factor related to the quality of the radiation. The weighted absorbed dose has been given the name dose equivalent by *ICRP* [1991]. The unit of dose equivalent is the Sievert (Sv). Dose equivalent in tissue T from particle j ($H_{j,T}(\mathbf{x})$) is defined in terms of the tissue LET-dependent quality factor Q, such that

$$H_{j,T}(\mathbf{x}) = \int_L Q(L) D_j(\mathbf{x}, L) dL, \quad (9)$$

where L is LET, which can be approximated by the stopping power in units of keV μm^{-1}; $D_j(\mathbf{x}, L)$ is the spectral dose distribution from particle j in terms of LET, and $Q(L)$ is the tissue LET-dependent quality factor.

[27] The relationship between the probability of biological damage and dose equivalent is found to also depend on the organ or tissue irradiated. A further dosimetric quantity, called the effective dose, is defined to include the relative contributions of each organ or tissue to the total biological detriment caused by radiation exposure. The effective dose ($E(\mathbf{x})$) is the sum of weighted dose equivalents in all the organs and tissues in the human body, such that

$$E(\mathbf{x}) = \sum_T \sum_j w_T H_{j,T}(\mathbf{x}). \quad (10)$$

The organ/tissue weighting factors are given in the ICRP 60 report [*ICRP*, 1991]. A computationally efficient approach is to calculate the effective dose rates directly from the particle spectral fluence rates using precomputed fluence-to-effective dose conversion coefficients. In this paper we use neutron and proton conversion coefficients tabulated by *Ferrari et al.* [1997a, 1997b]. The effective dose contributions from the other ions are obtained by scaling the proton fluence-to-effective dose conversion coefficients by Z_j^2/A_j, according to stopping power dependence on charge and mass. All recommended ICRP radiation exposure limits are defined in terms of effective dose.

[28] The assumptions and simplifications to our transport calculations and dosimetric predictions presented in section 4 are briefly described here. We assume that the incident SEP ion are isotropically distributed in angle, and we project the ions along the vertical direction to obtain the incident SEP spectral fluence rates in the calculation of effective dose in (8)–(10). Moreover, we assume the minimum access energies for the incident ions are determined by the vertical cutoff rigidities described in section 2.2. Finally, we ignore the influence of the aircraft structure on the radiation field. None of the existing atmospheric radiation models include aircraft structure effects operationally; however, some cases studies have been done. The aircraft may reduce the free atmosphere radiation exposure by perhaps ~10% for GCR exposure [*Battistoni et al.*, 2005; *Copeland et al.*, 2008] and less than 1% for SEP events [*Copeland et al.*, 2008]. Future updates to

NAIRAS will include transport through the aircraft fuselage, utilizing the methodologies developed for astronaut radiation risk assessment [*Badavi et al.*, 2007b; *Slaba et al.*, 2009], and quantify the directional effects on the cutoff rigidities and their subsequent influence on the radiation exposure.

4. Analysis of Halloween 2003 Event

[29] In this section we present our predictions of SEP effective dose rates and accumulated effective dose along representative high-latitude commercial routes during the Halloween 2003 SEP event 3 (29 October (2100 UT) to 31 October (2400 UT)). The incident SEP spectral fluence rates and meteorological data are fixed in time in our calculations, which are given by the event-averaged spectral fluence rates and atmospheric depth-altitude data shown in Figures 2 and 4, respectively. On the other hand, we allow the cutoff rigidity to vary in time along the flight trajectories, according to the magnetospheric magnetic field response to the real-time solar wind and IMF conditions [*Kress et al.*, 2010]. The physics-based HZETRN code is used to transport the incident SEP ions through the atmosphere and calculate the dosimetric quantities. A unique feature of NAIRAS is the computational efficiency of the deterministic HZETRN code and the ability to predict global atmospheric radiation exposure from a physics-based transport code. Moreover, the geomagnetic effects have not been quantified sufficiently in the past, and we find they have a profound effect on SEP atmospheric radiation exposure. In a future report, we will allow the SEP spectral fluence rates, cutoff rigidity, and atmospheric depth altitude to all vary according to the real-time data input.

4.1. Global SEP Dose Distribution

[30] Global SEP atmospheric ionizing radiation exposure are obtained from a precomputed database. The effective dose rates are calculated on a fixed 2-D grid in atmospheric depth and cutoff rigidity. The atmospheric depth grid extends from zero to 1300 g cm^{-2}, and the cutoff rigidity grid extends from zero to 19 GV. Both grids have nonuniform spacing with the highest number of grid points weighted toward low cutoff rigidities and tropospheric atmospheric depths. The real-time cutoff rigidities are computed on the same 2.5 × 2.5 horizontal grid as the NCEP/NCAR meteorological data. The precomputed effective dose rates are interpolated to the real-time cutoff rigidity and atmospheric depth specified at each horizontal grid point.

[31] Figure 5 shows global snapshots of atmospheric effective dose rates over the Northern Hemisphere polar region for the Halloween 2003 SEP event 3. The effective dose rates are shown at three altitudes and for three different magnetic field models used in the cutoff rigidity simulations. Figure 5 (left) shows exposure rates using the IGRF field. Figure 5 (middle) shows exposure rates computed for a geomagnetically quiet time prior to the onset of SEP event 3 using the T05 field (28 October 2003, 0002 UT). Figure 5 (right) shows the exposure rates using the T05 field at the peak of the geomagnetic storm (29 October 2003, 2100 UT) during SEP event 3. A typical cruising altitude for a commercial high-latitude flight is 11 km. Overlaid on the 11 km effective dose rate altitude surface are great circle routes for three representative high-latitude commercial flights: London, England (LHR) to New York, New York (JFK) (5.75 h flight time); Chicago, Illinois (ORD) to Stockholm, Sweden (ARN) (8.42 h flight time), and a combination of two great circle routes from Chicago, Illinois (ORD) to Beijing, China (PEK) (13.5 h flight time).

[32] There are a number of striking features to be noted from Figure 5. First, the representation of the geomagnetic field has a significant influence on SEP atmospheric ionizing radiation exposure. Comparing Figure 5 (left) and Figure 5 (middle) shows that even during geomagnetically quiet periods, the magnetospheric magnetic field weakens the overall geomagnetic field with a concomitant increase in radiation levels. This is seen as a broadening of the open-closed magnetospheric boundary in the T05 quiet field compared to the IGRF field. The cutoffs are zero in the region of open geomagnetic field lines. Thus, effective dose rates based on the IGRF field are underestimated even for magnetically quiet times. During strong geomagnetic storms, as shown in Figure 5 (right), the area of open field lines are broadened further, bringing large exposure rates to much lower latitudes. Effective dose rates predicted using the IGRF model during a large geomagnetic storm can be significantly underestimated. The expansion of the polar region high exposure rates to lower latitudes, due to geomagnetic effects, is quantified by calculating hemispheric average effective dose rates from 40N to the pole. This is denoted by "avg" in Figure 5. At 11 km, there is roughly an 8% increase in the global average effective dose rate using T05 quiet field compared to IGRF. During the geomagnetic storm, there is an ~30% increase in the global average effective dose rate using T05 storm field compared to IGRF.

[33] A second important feature to note in Figure 5 is the strong altitude dependence due to atmospheric shielding. The exposure rates are very low at 5 km, independent of geomagnetic field model used. At 15 km, the exposure rates are significantly higher than at 11 km. Figure 5 shows that the SEP effective dose rates increase (decrease) exponentially with increasing (decreasing) altitude. The SEP exposure rate altitude dependence is a fortunate feature for the aviation community, since radiation exposure can be significantly reduced by descending to lower altitudes. Private business jets will receive more radiation exposure than commercial aircraft if mitigation procedures are not taken, since business jet cruising altitudes are roughly 12–13 km. The altitude dependence of the SEP exposure rates is quantified in Figure 5 by showing the maximum effective dose rate at each altitude, which is the exposure rate at zero cutoff rigidity (i.e., in the polar region of open geomagnetic field lines). The maximum is denoted "max" in Figure 5. The exposure rate increases on average by

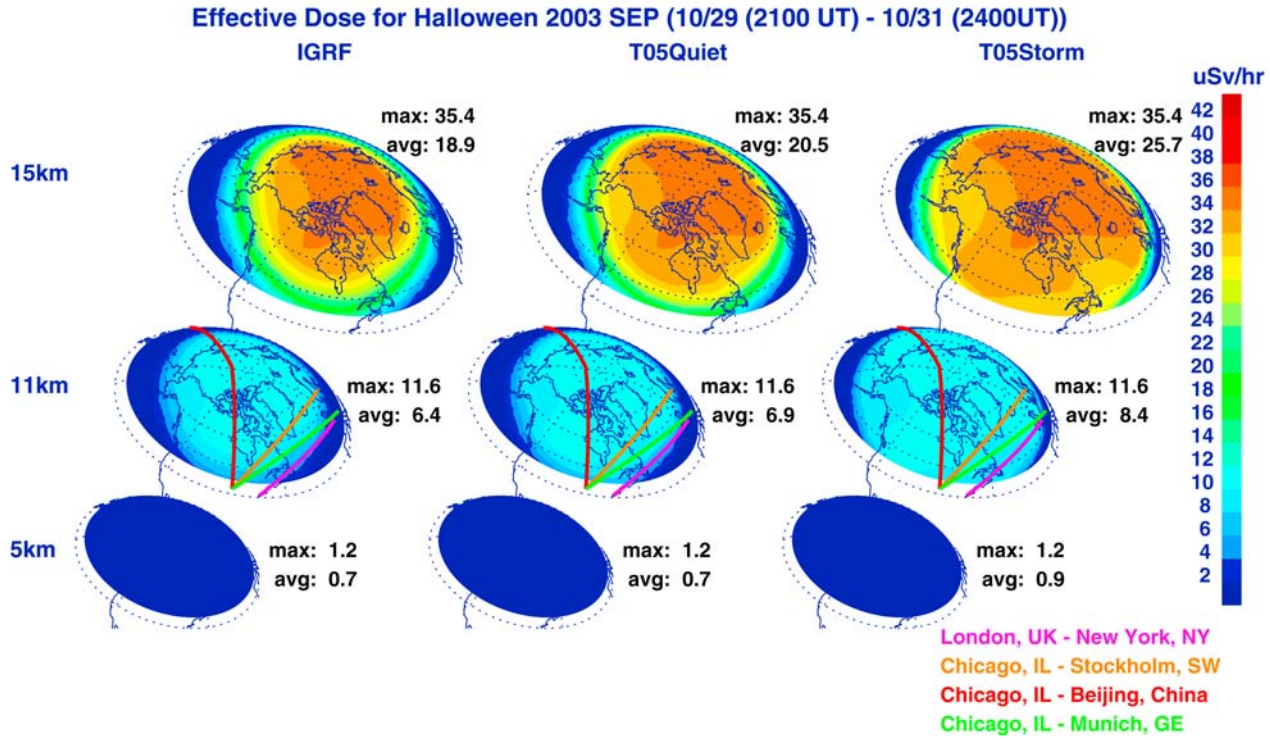

Figure 5. Effective dose rates computed during Halloween 2003 SEP event 3. (left, middle, and right) The plots correspond to exposure rates calculated using the geomagnetic cutoff rigidities and magnetic field models shown in Figure 3. (top, middle, and bottom) Exposure rates calculated at different altitudes. In each image, the hemispheric average effective dose rate (μSv h^{-1}) is indicated by the value next to "avg." The maximum exposure rate is indicated by the value next to "max." See text for definition of avg and max.

160% km^{-1} between 5 km and 11 km. Between 11 km and 15 km, the exposure rate increases on average by approximately 75% km^{-1}.

[34] It is instructive to compare our results to the 20 January 2005 SEP exposure rates computed by *Copeland et al.* [2008] using the Monte Carlo MCNPX transport code. Copeland et al. report maximum SEP effective doses of 0.045 mSv and 0.160 mSv at 30 kft (~9.1 km) and 40 kft (~12.2 km), respectively, for 1 h continuous exposure at zero cutoff rigidity. By interpolating these exposure rates linearly in log dose, we derive a maximum effective dose rate of 47 μSv h^{-1} at 11 km from the Copeland et al. results. This is a factor of 4 greater than our computed maximum effective dose rate shown in Figure 5 at 11 km for Halloween 2003 SEP event 3. According to the Copeland et al. study, the January 2005 SEP events produced the largest dose rates at aviation altitudes during solar cycle 23. On the other hand, Halloween 2003 SEP event 3 was associated with one of the five largest geomagnetic storms of solar cycle 23 [*Gopalswamy et al.*, 2005]. For our purpose of quantifying the geomagnetic storm effects on SEP exposure rates, the Halloween 2003 SEP event 3 provides an ideal storm period for our case study. This is discussed in more detail in section 4.2.

4.2. Dose on High-Latitude Flights

[35] Before calculating radiation exposure along specified flight paths, it is constructive to examine a sample of effective dose rate profiles at different cutoff rigidities from our precomputed database previously described for SEP event 3. Figure 6 shows SEP effective dose rates as a function of atmospheric depth for cutoff rigidities from zero to 2.5 GV. Figure 6 clearly shows the exponential dependence of SEP exposure on both cutoff rigidity and atmospheric depth. The vertical lines indicate constant exposure rates necessary to receive a total exposure of 1, 5, 10, and 20 mSv on an 8 h flight. A typical international, high-latitude flight is 8 h. The rationale for choosing the total exposure identified with the vertical lines is as follows [*Wilson et al.*, 2003]: 20 mSv is the ICRP annual occupational radiation worker limit, 10 mSv is the National Committee on Radiological Protection (NCRP) annual occupational exposure limit, 5 mSv is the NCRP occasional public exposure limit, and 1 mSv is the ICRP annual

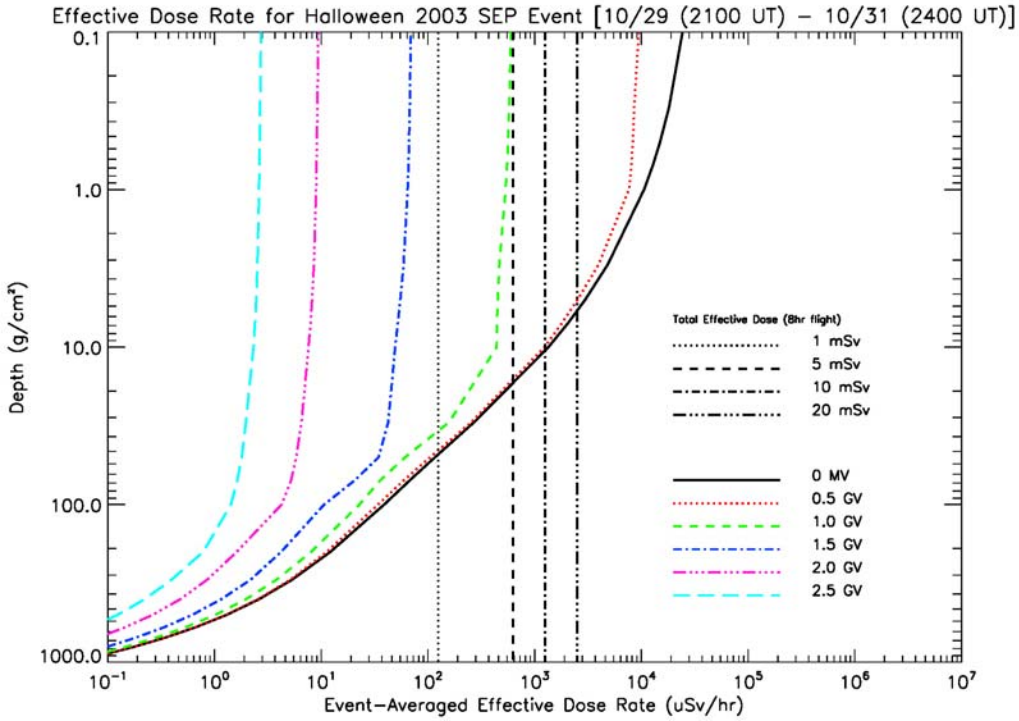

Figure 6. Event-averaged effective dose rates for Halloween SEP event 3 (29 October 2003 (2100 UT) to 31 October 2003 (2400 UT)) as a function of atmospheric depth for various geomagnetic cutoff rigidities. Different vertical lines indicate constant exposure rates required to reach the corresponding total exposure levels indicated in the legend for an 8 h flight.

public and prenatal exposure limit. The cutoff rigidities at high latitudes are less than 1 GV. The typical commercial airline cruising altitudes correspond to an atmospheric depth between ~200 and 300 g cm^{-2}. Consequently, one can see from Figure 6 that it is not possible for passengers on high-latitude commercial flights during the Halloween 2003 SEP events to approach or exceeded the ICRP public and/or prenatal radiation exposure limit.

[36] Figure 7 shows the cutoff rigidities and effective dose rates for the three representative high-latitude flights mentioned in section 4.1, which were calculated along great circle routes. Figure 7 (left) shows the cutoff rigidities along the flight paths, and Figure 7 (right) shows the corresponding effective dose rates along the flight paths. The cutoff rigidities include both latitude and time-dependent variations along the flight paths. The variations of the exposure rates along the flight paths include latitudinal variations in both atmospheric depth and cutoff rigidity. The temporal variations in cutoff rigidity also map into the variations of the exposure rates along the flight path. Figure 7 (top) shows results for the LHR-JFK flight, while Figure 7 (middle and bottom) shows results for the ORD-ARN and ORD-PEK flights. Each plot in Figure 7 shows cutoff rigidities and corresponding effective dose rates using the IGRF field (green lines) and the T05 storm field (red lines) in the cutoff calculations. The largest differences in flight path cutoff rigidities between IGRF and T05 storm field models are for the LHR-JFK flight. The entire LHR-JFK flight path is near the magnetosphere open-closed boundary and is most sensitive to perturbations in cutoff rigidity due to geomagnetic effects. Consequently, the exposure rates along the LHR-JFK flight are most sensitive to geomagnetic effects. The ORD-PEK polar route is the least sensitive to geomagnetic suppression of the cutoff rigidity, since most of the flight path is across the polar cap region with open geomagnetic field lines. The influence of geomagnetic storm effects on the ORD-ARN flight is intermediate between a typical polar route and a flight along the north Atlantic corridor between the US and Europe.

[37] The effective dose rates for the representative high-latitude flights in Figure 7 are within the range of exposure rates measured during other storm periods for similar flight paths. The measurement data were analyzed and reported in terms of ambient dose equivalent, which is a reasonable measurement proxy for effective dose. For example, *Clucas et al.* [2005] reported peak SEP dose rates in the 3.5–4.0 μSv h^{-1} range for a LHR-JFK flight on 14 July 2000, a SEP event without a concomitant geomagnetic storm. From Figure 7, the peak dose rate for the LHR-JFK

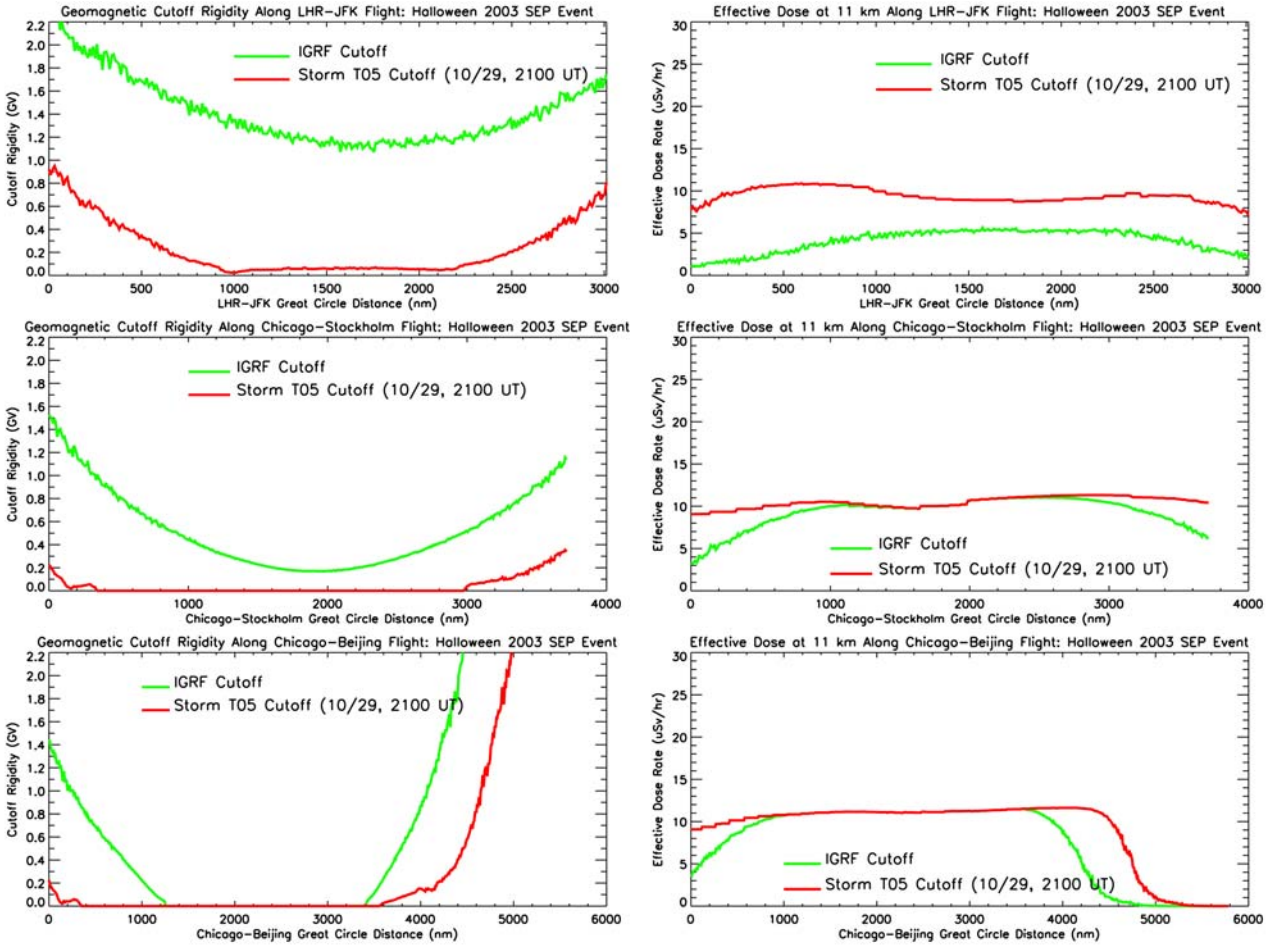

Figure 7. (left) Geomagnetic cutoff rigidities and (right) effective dose rates calculated during Halloween 2003 SEP event 3 along three representative flight paths for a cruising altitude of 11 km. The green line represents cutoff rigidities and exposure rates calculated using the IGRF model. The red lines represent cutoffs and exposure rates computed using the T05 model during the period of largest geomagnetic activity of event 3. The total flight times are the following: 5.75 h for JFK-LHR, 8.42 h for ORD-ARN, and 13.5 h for ORD-PEK.

flight computed using the IGRF field is ~4 μSv h^{-1}. Clucas et al. also showed peak measured SEP dose rates on the order of 10–12 μSv h^{-1} for a LHR-JFK flight during an April 2001 SEP event, which was accompanied by a geomagnetic storm. The average LHR-JFK effective dose rate in Figure 7 computed using the T05 storm field is 9.4 μSv h^{-1}. *Dyer et al.* [2005] reported measured peak SEP dose rates on the order of 9.5 μSv h^{-1} for a flight from Prague to New York during the April 2001 SEP event. Thus, our computed effective dose rates are in qualitative agreement with measured dose rates for similar flight paths during other storm periods.

[38] The high sensitivity of SEP atmospheric dose rates to geomagnetic conditions near the open-closed magnetospheric boundary is also responsible for the high sensitivity of SEP dose rates to the exact flight path in the north Atlantic corridor region. For example, *Dyer et al.* [2007] found that the differences in peak dose rates between great circle and actual flight paths for LHR-JFK Concorde flights were a factor of 5 during the September 1989 SEP event and a factor of 2.5 during the October 1989 event, which was geomagnetically quiet. Furthermore, the difference in peak SEP dose rates between great circle and actual flight paths for the commercial flight from Prague to New York during the April 2001 event was a factor of 2.

[39] The actual flight paths for the Chicago to Munich flights reported by *Beck et al.* [2005] may have been equatorward of a great circle route, which could explain their low dose rates compared to our calculated LHR-JFK great circle route dose rates during the Halloween 2003 superstorm. During the Halloween 2003 SEP event 3, the Chicago to Munich flight measured a mean SEP dose rate of 3.6 μSv h^{-1} and an accumulated dose of 0.032 mSv for the 8.75 h flight. These results are comparable to our

Table 2. Flight Path Effective Dose Using Different Geomagnetic Cutoff Models

Flight Path	Effective Dose T05S[a] (mSv)	Effective Dose T05Q[b] (mSv)	Effective Dose IGRF[c] (mSv)	Effective Dose Ratio T05S/IGRF	Effective Dose Ratio T05S/T05Q	Effective Dose Ratio T05Q/IGRF
JFK-LHR	0.054	0.030	0.024	2.25	1.18	1.25
ORD-ARN	0.088	0.084	0.078	1.13	1.05	1.08
ORD-PEK	0.122	0.116	0.102	1.20	1.05	1.14

[a]Cutoff rigidities computed from Tsyganenko (T05) storm fields.
[b]Cutoff rigidities computed from Tsyganenko (T05) quiet time fields.
[c]Cutoff rigidities computed from IGRF fields.

5.75 h JFK-LHR for geomagnetically quiet conditions presented in Figure 7 and Table 2. In other words, the Chicago to Munich flight did not seem to experience the dose rate enhancement due to the large geomagnetic storm. By comparing the LHR-JFK dose rates in Figure 7 computed using the IGRF field and the T05 storm field with the dose rates computed for the ORD-ARN and ORD-PEK flights, it is clear that geomagnetic effects enable flights along the North Atlantic corridor, or near the magnetosphere open-closed boundary, to experience the same dose rates that are confined to the polar region under geomagnetically quiet conditions.

[40] Another possible explanation for the relative difference in the Chicago to Munich measured dose rates reported by *Beck et al.* [2005] and our computed dose rates for the LHR-JFK flight is our use of the event-averaged incident SEP spectral fluence rate, which we employed for the purpose of isolating geomagnetic effects in our case study. It is clear from the shaded regions in Figure 2 that our event-averaged SEP spectra fluence rate is weighted more toward the peak ion flux measurements observed during SEP event 3. The measurements in Figure 1 show that the SEP ion flux rapidly decreased in time from the peak values present at the beginning of event 3. Thus, our use of an event-averaged incident SEP spectral fluence rate will tend to overestimate the accumulated effective dose over the flight paths in Figure 7. However, employing this constraint on the incident SEP spectral fluence rate is necessary to unambiguously isolate the geomagnetic effects. Despite these caveats, the results discussed in this paper are within the current factor of 2 uncertainty in SEP atmospheric dose rates [*Clucas et al.*, 2005].

[41] The total effective dose along the three representative high-latitude flight paths are given in Table 2. The second, third, and fourth columns show total effective dose computed from the three models of the geomagnetic field used in this study: IGRF, T05 quiet field, and T05 storm field. The last three columns show various ratios between the total effective dose computed from the different geomagnetic field models. There are three major points to be noted from these results. One, the total effective dose predicted for the ORD-PEK polar route for SEP event 3 during the Halloween 2003 storm is ~12% of the ICRP public/prenatal effective dose limit of 1 mSv. Passengers and crew on high-latitude flights during the Halloween 2003 SEP event 3 did not come close to approaching the recommended ICRP exposure limits. Two, using the IGRF field to compute the cutoff rigidity can underestimate the total effective dose from ~15% for polar routes to over a factor of 2 for flights along the north Atlantic corridor. Third, even for SEP events without an accompanying geomagnetic storm, using the IGRF field in cutoff rigidity simulations can underestimate the total effective dose by roughly 20%–30% for US flights into Europe.

[42] It is also instructive to compare the total effective dose for the ORD-PEK flight in Table 2 with result from *Copeland et al.* [2008] during the 20 January 2005 SEP event. Copeland et al. report maximum SEP effective doses of 0.088 mSv and 0.320 mSv at 30 kft and 40 kft, respectively, for 10 h of continuous exposure at zero cutoff rigidity. This corresponds to a total effective dose of 0.123 mSv at 11 km, which is nearly equal to the total effective dose for the 13.5 h ORD-PEK flight in Table 2. The average dose rates for the ORD-PEK flight in Table 2 are 9.0 μSv h^{-1} and 7.5 μSv h^{-1} for the T05 storm field and the IGRF field, respectively. Using these average dose rates to adjust the ORD-PEK total effective dose in Table 2 for a 10 h flight, we find the accumulated effective dose to be between 0.076 mSv and 0.091 mSv, which brings our result to within 25%–50% of the Copeland et al. result. Evidently, our use of the event-averaged incident SEP spectral fluence rate for the duration of a 10 h polar flight nearly compensates for the factor of 4 difference between the peak dose rate for the 20 January 2005 SEP event and event-averaged dose rate for the Halloween 2003 SEP event 3, as discussed in section 4.1.

[43] Another competing phenomena during the Halloween 2003 superstorm was the occurrence of several Forbush decreases [*Gopalswamy et al.*, 2005]. A Forbush decrease is a suppression of the GCR exposure due to the interaction of the solar wind with the incident GCR particles. At latitudes with cutoff rigidities greater than 1.0–1.2 GV, the SEP dose rates are comparable to or less than the GCR dose rates. Thus, at these latitudes, the total GCR+SEP dose rate can be less than the quiet time dose rates prior to the SEP event during a Forbush decrease. *Getley et al.* [2005a, 2005b] observed the apparent influence of a Forbush decrease on dosimetry measurements taken on Qantas Flight 107 from Los Angeles, California to New York, New York on 29 October 2003. These measurements are well suited for testing the ability of NAIRAS to model

the reduction in the GCR exposure due to Forbush decreases, which we plan to do in the future.

5. Summary and Conclusions

[44] The NAIRAS model is a physics-based, global, data-driven nowcast of atmospheric ionizing radiation, with radiation exposure rates calculated from the surface to approximately 100 km. At project completion, which is anticipated in mid-2011, NAIRAS will provide real-time predictions of radiation exposure for both background GCR and SEP events. In this paper we have conducted an analysis of atmospheric ionizing radiation exposure associated with a high-energy SEP event during the Halloween 2003 storm period. The main objective of this paper is to diagnose the influence of geomagnetic storm effects on SEP atmospheric radiation exposure. High-latitude flight paths are the routes most susceptible to significant SEP radiation exposure, since the cutoff rigidity rapidly approaches zero near the magnetosphere open-closed boundary.

[45] To achieve our objective of diagnosing the geomagnetic storm effects on SEP radiation exposure, we calculated the atmospheric effective dose rates using event-averaged incident SEP proton and alpha spectral fluence rates and a static atmospheric depth-altitude relation, while the cutoff rigidity was calculated both statically and dynamically. The static cutoff rigidities were simulated using the IGRF field. The dynamic cutoff rigidities were simulated using the T05 field, which was allowed to respond to the real-time solar wind and IMF conditions. The dynamic cutoff rigidities were computed during a geomagnetically quiet period prior to the high-energy SEP event and during the peak of the geomagnetic storm associated with the high-energy SEP event. The key results of this study are the following. One, ignoring solar wind–magnetosphere interactions during a strong geomagnetic storm, in the calculation of cutoff rigidities, can underestimate the total exposure by approximately 15% to over a factor of 2. Two, even during geomagnetically quiet conditions, ignoring solar wind–magnetosphere interactions can underestimate the total exposure for flights along the north Atlantic corridor by roughly 20%–30%. To achieve more accurate assessments of aircraft radiation dose, the magnetospheric influence on the cutoff rigidities must be included routinely in atmospheric radiation exposure predictions.

[46] We also showed that the SEP exposure rates increase (decrease) exponentially with increasing (decreasing) altitude. Thus, SEP aircraft radiation exposure can be significantly reduced by descending to lower altitudes. Business jet cruising altitudes are higher than commercial aircraft. Consequently, private jets flying similar high-latitude routes as the commercial airlines will receive substantially more radiation if mitigation procedures are not enacted. NAIRAS real-time radiation exposure rate predictions during SEP events will enable the aviation community to make informed decisions concerning radiation risk evaluation and reduction. The Halloween 2003 SEP events did not pose a radiation health risk, however.

[47] In the future, we will assess the reliability and feasibility of predicting the real-time geomagnetic cutoff rigidities using the physics-based LFM MHD magnetic fields. The LFM MHD code may be run as a stand alone model or coupled with other geospace models currently under development within CISM. For example, the LFM magnetospheric magnetic fields may be coupled with the Thermosphere-Ionosphere Nested Grid (TING) model [*Wang et al.*, 2004] and/or with the Rice Convection Model (RCM) [*Toffoletto et al.*, 2004], which models the ring current. The semiempirical T05 model provides more accurate cutoff rigidities than the stand alone LFM MHD model, as determined by comparisons with satellite observations during a Halloween 2003 geomagnetic storm [*Kress et al.*, 2010]. This is mainly due to the lack of a full kinetic description of the ring current in the MHD model, which typically causes the LFM fields to be too high. We anticipate that the fully coupled LFM-RCM-TING model currently under development will significantly improve the simulations of cutoff rigidities compared to the stand along LFM MHD model. Furthermore, the physics-based LFM-RCM-TING model will be able to incorporate short time scale dynamics not included in empirical magnetospheric magnetic field models. When the code development within CISM reaches sufficient maturity, we will assess the influence of short time scale magnetospheric dynamics on the atmospheric ionizing radiation field using the fully coupled LFM-RCM-TING model.

[48] Additionally, our future efforts will build upon this work in six other ways. One, we will study directional effects on the cutoff rigidities and subsequent radiation exposure rates. Two, we will model the aircraft fuselage in calculating radiation exposure. Three, we will allow the SEP spectral fluence rate and atmospheric pressure to vary with time according to the real-time input data. Four, we will analyze additional storm periods to further quantify the relative contributions of SEP spectral fluence rate, geomagnetic activity, and meteorological variability on atmospheric radiation exposure. Five, we will utilize real-time neutron monitor count rates to supplement the satellite ion flux measurements to better constrain the high-energy portion of the incident SEP spectral fluence rates beyond ~500 MeV n^{-1}. And six, we will compare our predictions with previous and future onboard aircraft dosimetric measurements.

[49] **Acknowledgments.** This work was supported by the NASA Applied Science Program. C.J.M. is grateful to Xiaojing Xu (SSAI, Inc.) for improving the graphics and for helpful discussions with Barbara Grajewski (National Institute for Occupational Safety and Health).

References

Aspholm, R., M.-L. Lindbohm, H. Paakkulainen, H. Taskinen, T. Nurminen, and A. Tiitinen (1999), Spontaneous abortions among Finnish flight attendants, *J. Occup. Environ. Med.*, *41*(6), 486–491.

Badavi, F. F., J. E. Nealy, G. de Angelis, J. W. Wilson, M. S. Clowdsley, N. J. Luetke, F. A. Cuncinotta, M. D. Weyland, and E. J. Semones (2005), Radiation environment and shielding model validation for CEV design, paper 2005-6651 presented at Space 2005, Am. Inst. of Aeronaut. and Astronaut., Long Beach, Calif., 30 Aug. to 1 Sept.

Badavi, F. F., J. K. Tramaglina, J. E. Nealy, and J. W. Wilson (2007a), Low Earth orbit radiation environments and shield model validation for ISS, paper 2007-6046 presented at Space 2007 Conference and Exposition, Am. Inst. of Aeronaut. and Astronaut., Long Beach, Calif., 18–20 Sept.

Badavi, F. F., C. R. Stewart-Sloan, M. A. Xapsos, J. L. Shinn, J. W. Wilson, and A. Hunter (2007b), Description of a generalized analytical model for the micro-dosimeter response, *NASA Tech. Rep., NASA/TP-2007-214886*.

Battistoni, G., A. Ferrari, M. Pelliccioni, and R. Villari (2005), Evaluation of the dose to aircrew members taking into consideration the aircraft structures, *Adv. Space Res.*, *36*, 1645–1652.

Beck, P., M. Latocha, S. Rollet, and G. Stehno (2005), TEPC reference measurements at aircraft altitudes during a solar storm, *Adv. Space Res.*, *36*, 1627–1633.

Brandt, S. (1999), *Data Analysis: Statistical and Computational Methods for Scientists and Engineers*, Springer, New York.

Clucas, S. N., C. S. Dyer, and F. Lei (2005), The radiation in the atmosphere during major solar particle events, *Adv. Space Res.*, *36*, 1657–1664.

Copeland, K., H. H. Sauer, F. E. Duke, and W. Friedberg (2008), Cosmic radiation exposure on aircraft occupants on simulated high-latitude flights during solar proton events from 1 January 1986 through 1 January 2008, *Adv. Space Res.*, *42*, 1008–1029.

Dyer, C., F. Lei, A. Hands, S. Clucas, and B. Jones (2005), Measurements of the atmospheric radiation environment from CREAM and comparisons with models for quiet time and solar particle events, *IEEE Trans. Nucl. Sci.*, *52*(6), 2326–2331.

Dyer, C., F. Lei, A. Hands, and P. Truscott (2007), Solar particle events in the QinetiQ Atmospheric Radiation Model, *IEEE Trans. Nucl. Sci.*, *54*(4), 1071–1075.

Ellison, D. C., and R. Ramaty (1985), Shock acceleration of electrons and ions in solar flares, *Astrophys. J.*, *298*, 400–408.

Ferrari, A., M. Pelliccioni, and M. Pillon (1997a), Fluence to effective dose conversion coefficients for neutrons up to 10 TeV, *Radiat. Prot. Dosim.*, *71*(3), 165–173.

Ferrari, A., M. Pelliccioni, and M. Pillon (1997b), Fluence to effective dose and effective dose equivalent conversion coefficients for protons from 5 MeV to 10 TeV, *Radiat. Prot. Dosim.*, *71*(2), 85–91.

Getley, I. L., M. L. Duldig, D. F. Smart, and M. A. Shea (2005a), Radiation dose along North American transcontinental flight paths during quiescent and disturbed geomagnetic conditions, *Space Weather*, *3*, S01004, doi:10.1029/2004SW000110.

Getley, I. L., M. L. Duldig, D. F. Smart, and M. A. Shea (2005b), The applicability of model based aircraft radiation dose estimates, *Adv. Space Res.*, *36*, 1638–1644.

Gold, R. E., S. M. Krimigis, S. E. Hawkins III, D. K. Haggerty, D. A. Lohr, E. Fiore, T. P. Armstrong, G. Holland, and L. J. Lanzerotti (1998), Electron, proton, and alpha monitor on the Advanced Composition Explorer spacecraft, *Space Sci. Rev.*, *86*, 541–562.

Gopalswamy, N., S. Yashiro, Y. Liu, G. Michalek, A. Vourlidas, M. L. Kaiser, and R. A. Howard (2005), Coronal mass ejections and other extreme characteristics of the 2003 October–November solar eruptions, *J. Geophys. Res.*, *110*, A09S15, doi:10.1029/2004JA010958.

Haggerty, D. K., E. C. Roelof, G. C. Ho, and R. E. Gold (2006), Quantitative comparison of ACE/EPAM data from different detector heads: Implications for NOAA RTSE users, *Adv. Space Res.*, *38*, 995–1000.

International Commission on Radiological Protection (ICRP) (1991), *Recommendations of the International Commission on Radiological Protection*, *Ann. ICRP*, *21*(1–3).

Kalnay, E., et al. (1996), The NCAR/NCEP 40-year reanalysis project, *Bull. Am. Meteorol. Soc.*, *77*, 437–471.

Kress, B. T., M. K. Hudson, K. L. Perry, and P. L. Slocum (2004), Dynamic modeling of geomagnetic cutoff for the 23–24 November 2001 solar energetic particle event, *Geophys. Res. Lett.*, *31*, L04808, doi:10.1029/2003GL018599.

Kress, B. T., C. J. Mertens, and M. Wiltberger (2010), Solar energetic particle cutoff variations during the 29–31 October 2003 geomagnetic storm, *Space Weather*, doi:10.1029/2009SW000488, in press.

Langlais, B., and M. Mandea (2000), An IGRF candidate geomagnetic field model for epoch 2000 and a secular variation model for 2000–2005, *Earth Planets Space*, *57*, 1137–1148.

Lauria, L., T. J. Ballard, M. Caldora, C. Mazzanti, and A. Verdecchia (2006), Reproductive disorders and pregnancy outcomes among female flight attendants, *Aviat. Space Environ. Med.*, *77*(7), 533–559.

Lewis, B. J., G. I. Bennett, A. R. Green, M. J. McCall, B. Ellaschuk, A. Butler, and M. Pierre (2002), Galactic and solar radiation exposure to aircrew during a solar cycle, *Radiat. Prot. Dosim.*, *102*(3), 207–227.

Lindborg, L., D. T. Bartlett, P. Beck, I. R. McAulay, K. Schnuer, H. Schraube, and F. Spurny (Eds.) (2004), *Cosmic Radiation Exposure of Aircraft Crew: Compilation of Measured and Calculated Data—A Report of EURADOS Working Group 5*, Eur. Com., Luxembourg.

Lyon, J. G., J. A. Fedder, and C. M. Mobarry (2004), The Lyon-Fedder-Mobarry (LFM) global MHD magnetospheric simulation code, *J. Atmos. Sol. Terr. Phys.*, *66*(15–16), 1333–1350.

McMeekin, R. R. (1990), Radiation exposure of air carrier crewmembers, *Advis. Circ. 120-52*, Fed. Aviat. Admin., Washington, D. C.

Mertens, C. J., J. W. Wilson, S. R. Blattnig, B. T. Kress, J. W. Norbury, M. J. Wiltberger, S. C. Solomon, W. K. Tobiska, and J. J. Murray (2008), Influence of space weather on aircraft ionizing radiation exposure, paper 2008-0463 presented at 46th Aerospace Sciences Meeting and Exhibit, Am. Inst. of Aeronaut. and Astronaut., Reno, Nev., 7–10 Jan.

Mewaldt, R. A., C. M. S. Cohen, A. W. Labrador, R. A. Leske, G. M. Mason, M. I. Desai, M. D. Looper, J. E. Mazur, R. S. Selesnick, and D. K. Haggerty (2005), Proton, helium, and electron spectra during the large solar particle events of October–November 2003, *J. Geophys. Res.*, *110*, A09S18, doi:10.1029/2005JA011038.

Nealy, J. E., F. A. Cucinotta, J. W. Wilson, F. F. Badavi, T. P. Dachev, B. T. Tomov, S. A. Walker, G. De Angelis, S. R. Blattnig, and W. Atwell (2007), Pre-engineering spaceflight validation of environmental models and the 2005 HZETRN simulations code, *Adv. Space Res.*, *4*, 1593–1610.

NOAA (2009), Solar Proton Events Affecting the Earth Environment, http://www.swpc.noaa.gov/ftpdir/indices/SPE.txt, Space Weather Predict. Cent., Boulder, Colo., 21 Sept.

O'Brien, K., W. Friedberg, D. F. Smart, and H. H. Sauer (1998), The atmospheric cosmic- and solar energetic particle radiation environment at aircraft altitudes, *Adv. Space Res.*, *21*, 1739–1748.

O'Brien, K., D. F. Smart, M. A. Shea, E. Felsberger, U. Schrewe, W. Friedberg, and K. Copeland (2003), World-wide radiation dose-age calculations for air crew members, *Adv. Space Res.*, *31*, 835–840.

Onsager, T. G., et al. (1996), Operational uses of the GOES energetic particle detectors, in *GOES-8 and Beyond*, edited by E. R. Washwell, *Proc. SPIE Int. Soc. Opt. Eng.*, *2812*, 281–290.

Picone, J. M., A. E. Hedin, D. P. Drob, and A. C. Aikin (2002), NRLMSIS-00 empirical model of the atmosphere: Statistical comparisons and scientific issues, *J. Geophys. Res.*, *107*(A12), 1468, doi:10.1029/2002JA009430.

Schraube, H., V. Mares, S. Roesler, and W. Heinrich (1999), Experimental verification and calculation of aviation route doses, *Radiat. Prot. Dosim.*, *86*(4), 309–315.

Slaba, T. C., G. D. Qualls, M. S. Clowdsley, S. R. Blattnig, L. C. Simonsen, S. A. Walter, and R. C. Singleterry (2009), Analysis of mass averaged tissue doses in CAM, CAF, MAX, and FAX, *NASA Tech. Rep., NASA/TP-2009-215562*.

Smart, D. F., and M. A. Shea (1994), Geomagnetic cutoffs: A review for space dosimetry calculations, *Adv. Space Res.*, *14*, 10,787–10,796.

Smart, D. F., and M. A. Shea (2005), A review of geomagnetic cutoff rigidities for Earth-orbiting spacecraft, *Adv. Space Res.*, *36*, 2012–2020.

Toffoletto, F. R., S. Sazykin, R. W. Spiro, R. A. Wolf, and J. G. Lyon (2004), RCM meets LFM: Initial results of one-way coupling, *J. Atmos. Sol. Terr. Phys.*, *66*(15–16), 1361–1370.

Tsyganenko, N. A., and M. I. Sitnov (2005), Modeling the dynamics of the inner magnetosphere during strong geomagnetic storms, *J. Geophys. Res.*, *110*, A03208, doi:10.1029/2004JA010798.

Tylka, A. J., and M. A. Lee (2006), Spectral and compositional characteristics of gradual and impulsive solar energetic particle events,

in *Solar Eruptions and Energetic Particles*, *Geophys. Monogr. Ser.*, vol. 165, edited by N. Gopalswamy, R. Mewaldt, and J. Torsti, pp. 263–274, AGU, Washington, D. C.

Tylka, A. J., C. M. S. Cohen, W. F. Dietrich, M. A. Lee, C. G. Maclennan, R. A. Mewaldt, C. K. Ng, and D. V. Reames (2005), Shock geometry, seed populations, and the origin of variable elemental composition at high energies in large gradual solar particle events, *Astrophys. J.*, *625*, 474–495.

Wang, W., M. Wiltberger, A. G. Burns, S. C. Solomon, T. L. Killeen, N. Maruyama, and J. G. Lyon (2004), Initial results from the coupled magnetosphere-ionosphere-thermosphere model: Thermosphere-ionosphere responses, *J. Atmos. Sol. Terr. Phys.*, *66*(15–16), 1425–1441.

Waters, M., T. F. Bloom, and B. Grajewski (2000), The NIOSH/FAA working women's health study: Evaluation of the cosmic-radiation exposures of flight attendants, *Health Phys.*, *79*(5), 553–559.

Wilson, J. W., L. W. Townsend, W. Schimmerling, G. S. Khandelwal, F. Khan, J. E. Nealy, F. A. Cucinotta, L. C. Simonsen, J. L. Shinn, and J. W. Norbury (1991), Transport methods and interactions for space radiations, *NASA Tech. Rep., NASA-RP-1257*.

Wilson, J. W., I. W. Joes, D. L. Maiden, and P. Goldhagan (Eds.) (2003), Atmospheric Ionizing Radiation (AIR): Analysis, results, and lessons learned from the June 1997 ER-2 campaign, *NASA Conf. Publ., NASA/CP-2003-212155*.

Wilson, J. W., J. Tweed, S. A. Walker, F. A. Cucinotta, R. K. Tripathi, S. Blattnig, and C. J. Mertens (2005a), A procedure for benchmarking laboratory exposures with 1 A GeV iron ions, *Adv. Space Res.*, *35*, 185–193.

Wilson, J. W., C. J. Mertens, P. Goldhagan, W. Friedberg, G. De Angelis, J. M. Clem, K. Copeland, and H. B. Bidasaria (2005b), Atmospheric ionizing radiation and human exposure, *NASA Tech. Rep., NASA/TP-2005-213935*.

Wilson, J. W., R. K. Tripathi, C. J. Mertens, S. R. Blattnig, M. S. Clowdsley, F. A. Cucinotta, J. Tweed, J. H. Heinbockel, S. A. Walker, and J. E. Nealy (2005c), Verification and validation: High charge and energy (HZE) transport codes and future development, *NASA Tech. Rep., NASA/TP-2005-213784*.

Wilson, J. W., et al. (2006), International space station: A testbed for experimental and computational dosimetry, *Adv. Space Res.*, *37*, 1656–1663.

S. R. Blattnig and T. S. Slaba, NASA Langley Research Center, 2 West Reid St., Mail Stop 188E, Hampton, VA 23681-2199, USA. (steve.r.blattnig@nasa.gov; tony.c.slaba@nasa.gov)

M. Engel, Department of Physics, Hamline University, 1536 Hewitt Ave., Mail Stop B1807, Saint Paul, MN 55104-1205, USA. (mengel02@hamlineuniversity.edu)

B. T. Kress, Department of Physics and Astronomy, Dartmouth College, HB 6127 Wilder Laboratory, Hanover, NH 03755-3528, USA. (bkress@darmouth.edu)

C. J. Mertens, NASA Langley Research Center, 21 Langley Blvd., Mail Stop 401B, Hampton, VA 23681-2199, USA. (christopher.j.mertens@nasa.gov)

S. C. Solomon and M. Wiltberger, High Altitude Observatory, National Center for Atmospheric Research, 3080 Center Green, Boulder, CO 80307, USA. (stans@ucar.edu; wiltbemj@ucar.edu)